

# Oscillations and mass-draining that lead to a sympathetic eruption of a quiescent filament

JUN DAI,<sup>1,2</sup> QINGMIN ZHANG,<sup>1,2</sup> YANJIE ZHANG,<sup>1,2</sup> ZHE XU,<sup>1,2</sup> YINGNA SU,<sup>1,2</sup> AND HAISHENG JI<sup>1,2</sup>

<sup>1</sup>Key Laboratory of Dark Matter and Space Astronomy, Purple Mountain Observatory, CAS, Nanjing, 210023, People's Republic of China

<sup>2</sup>School of Astronomy and Space Science, University of Science and Technology of China, Hefei, 230026, People's Republic of China

(Received December 8, 2021; Revised December 8, 2021; Accepted December 8, 2021)

Submitted to ApJ

## ABSTRACT

In this paper, we present a multi-wavelength analysis to mass-draining and oscillations in a large quiescent filament prior to its successful eruption on 2015 April 28. The eruption of a smaller filament that was parallel and in close,  $\sim 350''$  proximity was observed to induce longitudinal oscillations and enhance mass-draining within the filament of interest. The longitudinal oscillation with an amplitude of  $\sim 25$  Mm and  $\sim 23$  km s<sup>-1</sup> underwent no damping during its observable cycle. Subsequently the slightly enhanced draining may have excited a eruption behind the limb, leading to a feedback that further enhanced the draining and induced simultaneous oscillations within the filament of interest. We find significant damping for these simultaneous oscillations, where the transverse oscillations proceeded with the amplitudes of  $\sim 15$  Mm and  $\sim 14$  km s<sup>-1</sup>, while the longitudinal oscillations involved a larger displacement and velocity amplitude ( $\sim 57$  Mm,  $\sim 43$  km s<sup>-1</sup>). The second grouping of oscillations lasted for  $\sim 2$  cycles and had the similar period of  $\sim 2$  hours. From this, the curvature radius and transverse magnetic field strength of the magnetic dips supporting the filaments can be estimated to be  $\sim 355$  Mm and  $\geq 34$  G. The mass-draining within the filament of interest lasted for  $\sim 14$  hours. The apparent velocity grew from  $\sim 35$  km s<sup>-1</sup> to  $\sim 85$  km s<sup>-1</sup>, with the transition being coincident with the occurrence of the oscillations. We conclude that two filament eruptions are sympathetic, i.e. the eruption of the quiescent filament was triggered by the eruption of the nearby smaller filament.

**Keywords:** Sun: filaments, prominences — Sun: Oscillations — Sun: coronal mass ejections (CMEs)

## 1. INTRODUCTION

Solar filaments are features filled with cool and dense plasma suspended in the corona (Labrosse et al. 2010; Mackay et al. 2010; Régnier et al. 2011). They usually form along the magnetic polarity inversion lines (PILs) and can be erupted (van Ballegooijen & Martens 1989; Martin 1998; Gibson 2018). Frequently, two adjoining filaments could erupt successively. This kind of phenomenon is termed as a sympathetic eruption. The sympathetic eruptions appear to occur sequentially over relatively short periods of time, across separated source regions (Liu et al. 2009), and sometimes even across a full hemisphere (Zhukov & Veselovsky 2007). They are usually interlinked by large-scale background magnetic

fields (Cheng et al. 2005; Schrijver & Title 2011; Titov et al. 2012; Schrijver et al. 2013), and physical connections of magnetic nature between sympathetic eruptions have been confirmed by statistical analysis (Moon et al. 2002; Wheatland & Craig 2006) and case studies (Wang et al. 2001; Ding et al. 2006; Wang et al. 2016). Generally, coronal mass ejections (CMEs), extreme ultraviolet (EUV) waves, and the propagating perturbations along magnetic field can cause sympathetic eruptions (Wang et al. 2001; Jiang et al. 2008; Török et al. 2011; Lynch & Edmondson 2013; Jin et al. 2016). In certain case of sympathetic eruptions between multiple filaments, the physical connection is interpreted as the magnetic reconnection between the overlying magnetic field (Török et al. 2011; Shen et al. 2012; Wang et al. 2018; Song et al. 2020; Hou et al. 2020).

Apparently, single filament eruption is more common than sympathetic eruptions. Since the filaments are

highly dynamic, the destabilization of a filament may lead to an eruption as a result of magnetic reconnection or ideal magnetohydrodynamic (MHD) instabilities (Forbes et al. 2006; Chen 2011; Janvier et al. 2015). Moreover, the total mass of a filament reaches up to  $10^{14}$ – $10^{15}$  g (Parenti 2014), and the mass of a filament is believed to be important for its stabilization (Zhang et al. 2021). Low (1996) proposed that the decrease in weight could cause a filament to rise up and finally erupt. Using simultaneous observations in  $H\alpha$  and  $He\text{ I }10830\text{ \AA}$ , Gilbert et al. (2001) observed fragmentary disappearance of a filament as the plasma flows onto the disk. The stereoscopic observation on 2010 April 3 shows that the slow uplift and eruption of the filament are induced by mass-unloading (Seaton et al. 2011). Recently, Jenkins et al. (2018) also presented an analysis for stereoscopic observation of the partial eruption of a quiescent prominence and concluded that impulsive mass-unloading is responsible for the eruption. Moreover, Jenkins et al. (2019) modeled a simple flux rope to quantify the effect of mass-draining in a filament. It is revealed that the rapid depletion of mass before the loss of equilibrium facilitates the increase in height of the flux rope. Fan (2020) performed 3D MHD numerical simulations for mass-unloading in a filament, they found that the presence of mass within the flux rope lead to an increase in the height required for loss-of-equilibrium and mass-draining can cause an earlier eruption by  $\sim 6$  hr. These observations and numerical simulations suggest that mass-draining may play an important role in the filament eruption.

Apart from mass-draining, a filament will exhibit various kinds of oscillatory motions when it is being disturbed (Ballester 2006; Oliver 2009; Tripathi et al. 2009; Arregui et al. 2018). According to the velocity amplitude, filament oscillations are generally classified as small-amplitude ( $\leq 10\text{ km s}^{-1}$ ) and large-amplitude ( $\geq 20\text{ km s}^{-1}$ ) oscillations (Oliver & Ballester 2002; Luna et al. 2018). Depending on their directions, the large-amplitude oscillations (LAOs) are further divided into large-amplitude transverse oscillations (LATOs) perpendicular to the axis of a corresponding filament and large-amplitude longitudinal oscillations (LALOs) along the axis. Generally, LATOs are triggered by global magnetohydrodynamic (MHD) waves or shock waves, such as chromospheric Moreton waves (Moreton & Ramsey 1960) and coronal EUV waves (Okamoto et al. 2004), which are closely associated with remote flares or CMEs (Hyder 1966; Ramsey & Smith 1966; Bocchialini et al. 2011; Liu et al. 2013; Shen et al. 2014a, 2017; Zhang & Ji 2018). In a particular case, slow rise or pre-eruption of a nearby erupting filament could also excite LATOs

(Isobe & Tripathi 2006; Isobe et al. 2007; Pintér et al. 2008; Chen et al. 2008). The magnetic tension is theoretically considered as the main restoring force for LATOs, and the damping is usually due to the energy loss or dissipative process (Kleczeck & Kuperus 1969; Tripathi et al. 2009). LALOs are mostly triggered by solar flares adjacent to the filaments footpoints (Jing et al. 2003, 2006; Vršnak et al. 2007; Li & Zhang 2012; Zhang et al. 2012, 2017b, 2020) or by coronal jets (Luna et al. 2014; Zhang et al. 2017a; Luna & Moreno-Insertis 2021). Sometimes, LALOs could be triggered by coronal shock waves during flares (Shen et al. 2014b; Pant et al. 2015) or by the merging of two adjacent filaments (Luna et al. 2017). The predominant restoring force of LALOs is believed to be the projected gravity along the flux tube supporting the filament threads (Luna et al. 2012; Zhang et al. 2012; Zhou et al. 2017). The primary damping mechanisms for LALOs include mass accretion (Luna & Karpen 2012; Ruderman & Luna 2016; Awasthi et al. 2019), radiative loss (Zhang et al. 2013), and wave leakage (Zhang et al. 2019). A simulation shows that mass drainage reduces the damping time considerably in one strong perturbation (Zhang et al. 2013). Recent numerical simulations have shed light on the nature of large-amplitude longitudinal oscillations (e.g., Terradas et al. 2015; Zhou et al. 2018; Adrover-González & Terradas 2020; Liakh et al. 2020, 2021).

LAOs before eruptions are frequently observed, showing that filament oscillation can serve as a kind of precursor for subsequent eruption (Chen et al. 2008; Zhang et al. 2012). Bi et al. (2014) presented early reports of both LATOs and mass-draining preceding a filament eruption, and the similar processes have been nicely reproduced with 3D numerical simulations (Fan 2020). However, questions like whether there is a mutual facilitation between the filament oscillation and mass-draining, and whether both contribute to the triggering a filament eruption are still unclear and need more analysis with well-observed cases.

On 2015 April 28, a sympathetic successful filament eruption induced by a nearby filament eruption occurred in the northeast hemisphere of the Sun. For the same event, Lörinčík et al. (2021) studied the plasma outflows originating in the coronal dimming after the sympathetic eruption. In this paper, we focus on the oscillations and the mass-draining before the successful eruption. The observation and data analysis are described in Section 2. The results are presented in Section 3. A comparison with previous findings and a brief conclusion are given in Section 4.

## 2. OBSERVATION AND DATA ANALYSIS

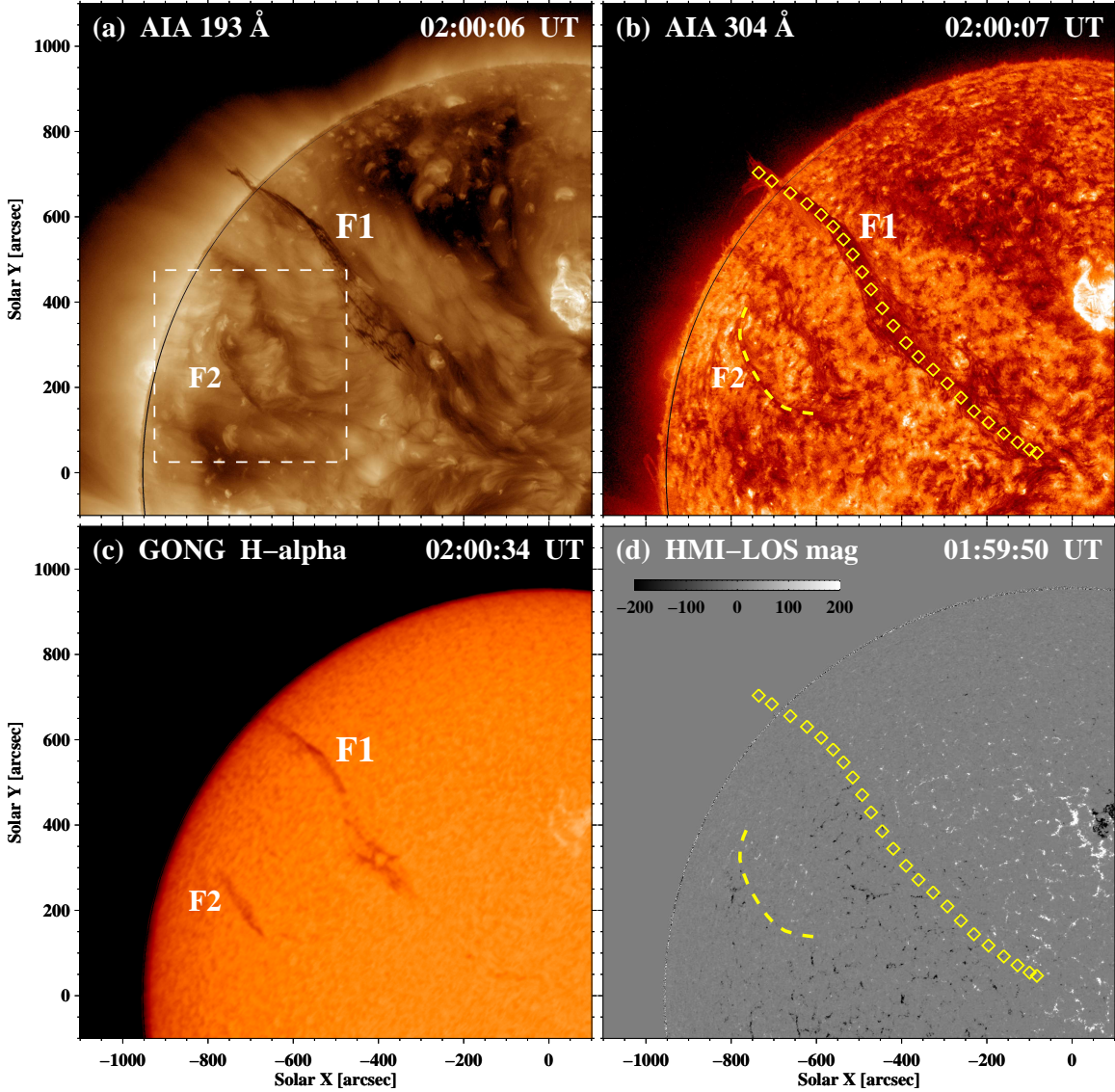


**Figure 1.** The appearance of the two filaments labeled as F1 and F2 in AIA 193 Å (a), 304 Å (b) and H $\alpha$  (c) images. Yellow dashed line outlines F2 and the yellow diamonds outline F1. Panel (d) give an HMI LOS magnetogram with the magnetic field strengths in the range of -200 and 200 G. The white rectangle in panel (a) gives the field of view (FOV) of Figure 2.

On 2015 April 28, two quiescent filaments, located in the northeast quadrant of the solar disk, were simultaneously observed by the Global Oscillation Network Group (GONG) in H $\alpha$  line center (6562.8 Å) and by the Atmospheric Imaging Assembly (AIA; [Lemen et al. 2012](#)) on board the Solar Dynamics Observatory (SDO; [Pesnell et al. 2012](#)). The full-disk H $\alpha$  images have a cadence of 60 s and a spatial resolution of 2". AIA takes full-disk images in two ultraviolet (UV; 1600 and 1700 Å) wavelengths with a cadence of 24 s and in seven EUV (94, 131, 171, 193, 211, 304, and 335 Å) wavelengths with a cadence of 12 s. The photospheric line-of-sight (LOS) magnetograms were observed by the Helioseismic and Magnetic Imager (HMI; [Schou et al. 2012](#)) on

board SDO with a cadence of 45 s. The level\_1 data from AIA and HMI with a spatial resolution of 1".2 were calibrated using the standard Solar SoftWare (SSW) programs `aia_prep.pro` and `hmi_prep.pro`. The images observed in H $\alpha$  and 304 Å were co-aligned with the cross-correlation method using sunspots as references. The large-scale 3D magnetic configuration near the filaments was derived from the potential field source surface (PFSS; [Schrijver & De Rosa 2003](#)) modeling. The associated CMEs were observed by the C2 on board the SOHO Large Angle and Spectrometric Coronagraph (LASCO; [Brueckner et al. 1995](#)).

### 3. RESULTS



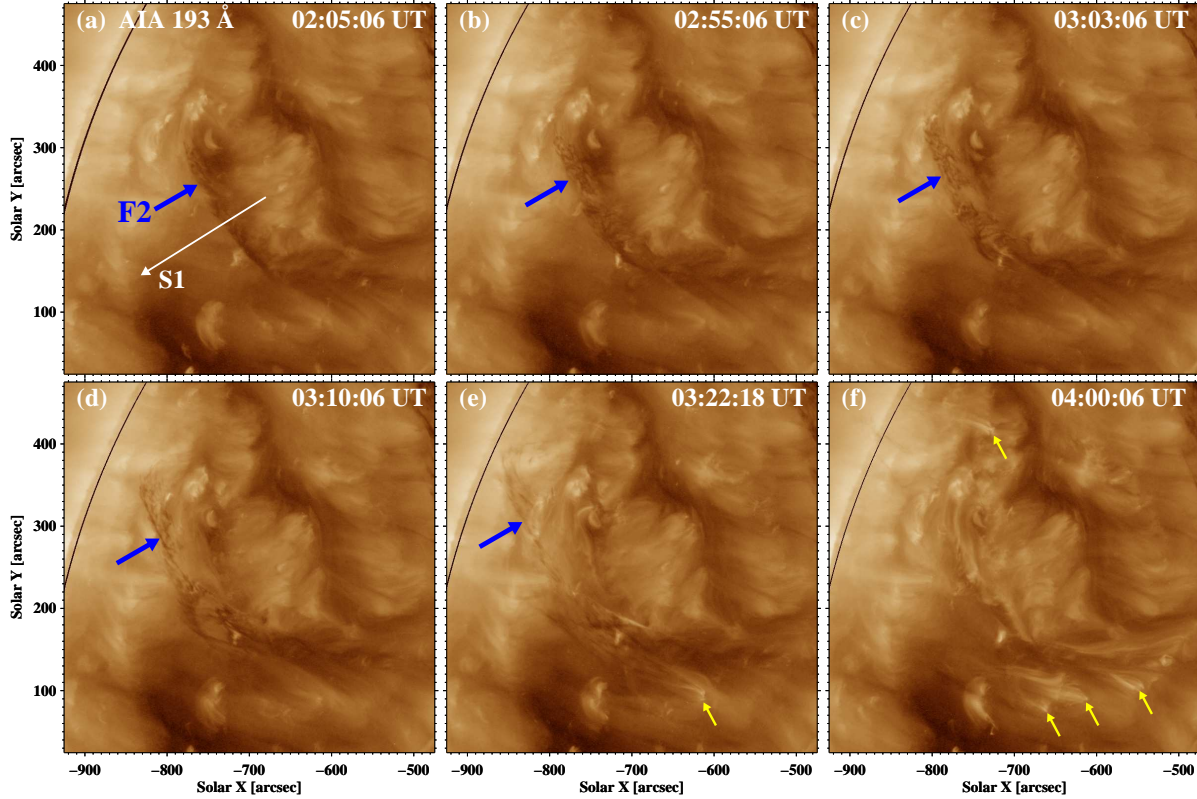


**Figure 2.** Six snapshots of the AIA 193 Å images, showing the temporal evolution of the eruption of F2. The blue arrows point to the spine of F2, and the yellow arrows point to the brightenings at the footpoints of F2. In panel (a), the white slice S1 is used to investigate the height evolution of F2. An animation (*F2eruption.mp4*) of the unannotated SDO observations is available. *F2eruption.mp4* covers  $\sim 4$  hr starting at 00:59:54 UT and ending the same day at 04:55:30 UT, with time cadence of 24 seconds. The FOV is displayed by the white rectangle in Figure 1(a) (An animation of this figure is available.)

### 3.1. F2 eruption and another eruption

In Figure 1, the top panels show EUV images in 193 Å and 304 Å at  $\sim 02:00:06$  UT. The bottom left panel shows the  $H\alpha$  image at 02:00:34 UT with the same field of view (FOV). Two parallel quiescent filaments (F1 and F2) are clearly seen and F1 is much longer than F2. The distance between the two filaments is  $\sim 350''$ . Figure 1(d) shows the photospheric LOS magnetogram at 01:59:50 UT, with the spines of F1 and F2 being marked with a series of yellow diamonds and a dashed line, respectively. It is clear that both filaments are located along PILs.

From 02:00 UT to 15:00 UT, F2 and F1 erupted successively, which could be considered as two separate eruptions due to the long time span. In addition, there was another filament eruption behind F1 during 06:00–08:00 UT (see also the online animation *F1eruption.mp4*), which is labeled as Eruption3 in Figure 4(a). Figure 2 shows six snapshots of EUV images in 193 Å during 02:00–04:00 UT, where the spine of F2 is indicated by the blue arrows (see also the online animation *F2eruption.mp4*). It shows that F2 rose slowly

from  $\sim 01:05$  UT and reached its eruption apex at  $\sim 03:20$  UT. The erupted material appears to have fallen back towards the two footpoints and caused brightenings, as indicated by the yellow arrows in Figure 2(e-f). Hence, F2 may be defined as a failed eruption (Ji et al. 2003; Dai et al. 2021). However, the presence of a weak associated CME can be identified within the LASCO/C2 snapshots of Figure 7 (a1-a3), indicating this was in fact a successful eruption.

To investigate the height evolution of F2, we select a straight slice (S1) with a length of  $179''$  along the eruption direction in Figure 2(a). The time-space diagram of S1 in 193 Å is plotted in Figure 5(a) and the height of F2 can be obtained by outlining the edge in the the diagram. The height evolution in the plane-of-sky is characterized by a slow rise with a constant speed followed by an initial impulsive acceleration **indicated** by an apparent exponential increase. Hence, we fit  $h(t)$  using the function as proposed by Cheng et al. (2013):

$$h(t) = c_0 e^{(t-t_0)/\tau} + c_1(t-t_0) + c_2, \quad (1)$$

where  $t_0$ ,  $\tau$ ,  $c_0$ ,  $c_1$ , and  $c_2$  are free parameters. This model is composed of a linear term and an exponen-

**Table 1.** Fitted parameters for longitudinal and transverse filament oscillations.

|     | $t_{sta}$<br>(UT) | $t_{end}$<br>(UT) | $A_0$<br>(Mm) | $P$<br>(min) | $\tau$<br>(min) | $\tau/P$ | $v_{max}$<br>(km s <sup>-1</sup> ) |
|-----|-------------------|-------------------|---------------|--------------|-----------------|----------|------------------------------------|
| OS1 | 03:35             | 07:10             | 25.1          | 114          | ...             | ...      | 23                                 |
| OS2 | 06:05             | 10:25             | 57.5          | 142          | 230             | 1.6      | 46                                 |
| OS3 | 07:20             | 10:35             | 56.9          | 126          | 168             | 1.3      | 41                                 |
| OS4 | 06:05             | 09:55             | 14.7          | 105          | 142             | 1.4      | 14                                 |

tial term, which correspond to the slow rise and the impulsive acceleration phase, respectively. The exponential term is reasonable, since it describes the impulsive acceleration of the filament when it is triggered by the flare reconnection (e.g., Moore et al. 2001) or the MHD instability (e.g., Török & Kliem 2005). The onset of fast-rise phase is defined by setting the parameters as the point when the exponential velocity is equal to the linear velocity:

$$t_{onset} = \tau \ln(c_1 \tau / c_0) + t_0. \quad (2)$$

The fitting process is implemented by the standard SSW program `mpfit.pro` and the fitted curve is plotted with the yellow solid line in Figure 5(a). It is clear that the fitted curve can nicely represent the height evolution of F2. The spine of F2 started to rise slowly from  $\sim 01:05$  UT at a speed of  $\sim 2$  km s<sup>-1</sup>. The fast rise began at  $\sim 02:30$  UT and lasted for  $\sim 50$  minutes with an average speed of  $\sim 85$  km s<sup>-1</sup>.

### 3.2. Oscillations in F1

After the cool material in F2 fell back to the footpoints at  $\sim 03:35$  UT, the threads in F1 began to oscillate along its axial direction, which is indicated by white arrows in Figure 3(a2-a3) (see also the online movie *OSandDR.mp4*). To investigate the longitudinal oscillations and whether there are transverse oscillations in F1, we select a straight slice (S2) along the axis with a length of  $421''$  and another straight slice S3 perpendicular to the axis with a length of  $180''$  in Figure 4(b), and the two time-space diagrams in  $211 \text{ \AA}$  are plotted in Figure 5(b-c). Surprisingly, we find a set of transverse oscillating signals, which is obviously damping. The transverse damping oscillation (OS4) during 06:05–09:55 UT is drawn with white pluses in Figure 5(c). In addition, we find three sets of longitudinal oscillating signals, two are damping while one has no obvious damping (non-damping). The non-damping oscillation (OS1) lasts for  $\sim 2$  cycles during 03:35–07:10 UT is drawn with white pluses. The damping oscillations (OS2 and OS3) are drawn with blue and yellow pluses, respectively. The simultaneous oscillations (i.e. OS2 and OS4) start almost at the same time ( $\sim 06:05$  UT) and both fade out after going through  $\sim 2$  cycles. The OS3 lags behind

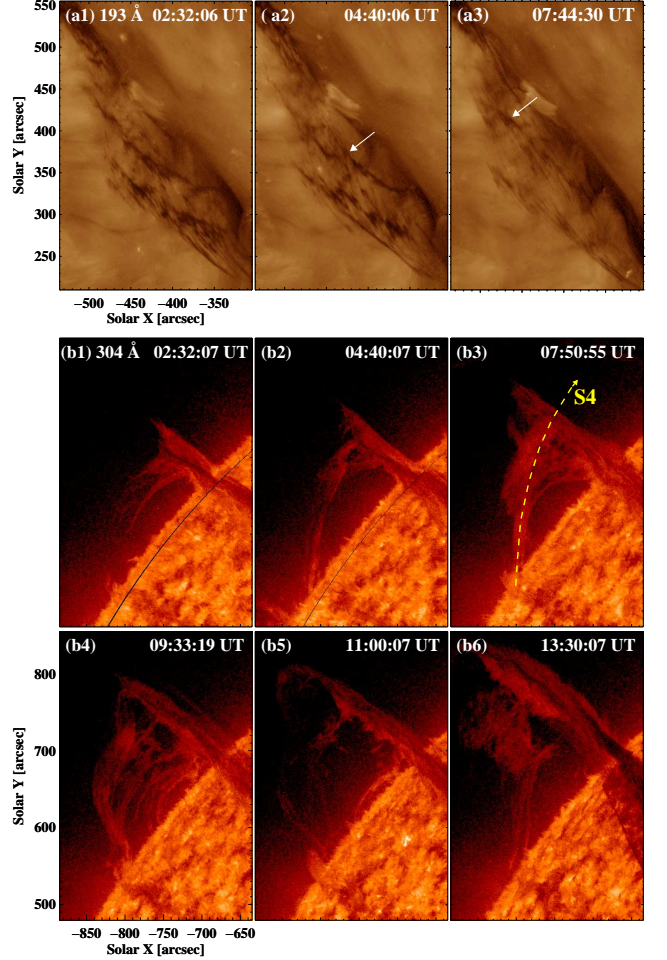


**Figure 3.** Panels (a1-a3) give three AIA 193 Å images, showing the longitudinal oscillations in F1. The white arrows point to an oscillating thread. Panel (b1-b6) give six snapshots of AIA 304 Å images, showing the mass-draining toward the solar surface along the barb. The curved slice S4 is used to investigate the mass-draining. An animation (*OSandDR.mp4*) of the unannotated SDO observations is available. *OSandDR.mp4* covers  $\sim 13$  hr starting at 01:00:18 UT and ending the same day at 13:59:55 UT, with time cadence of 1 minute. The FOV is displayed by the white rectangles in Figure 4(b). (An animation of this figure is available.)



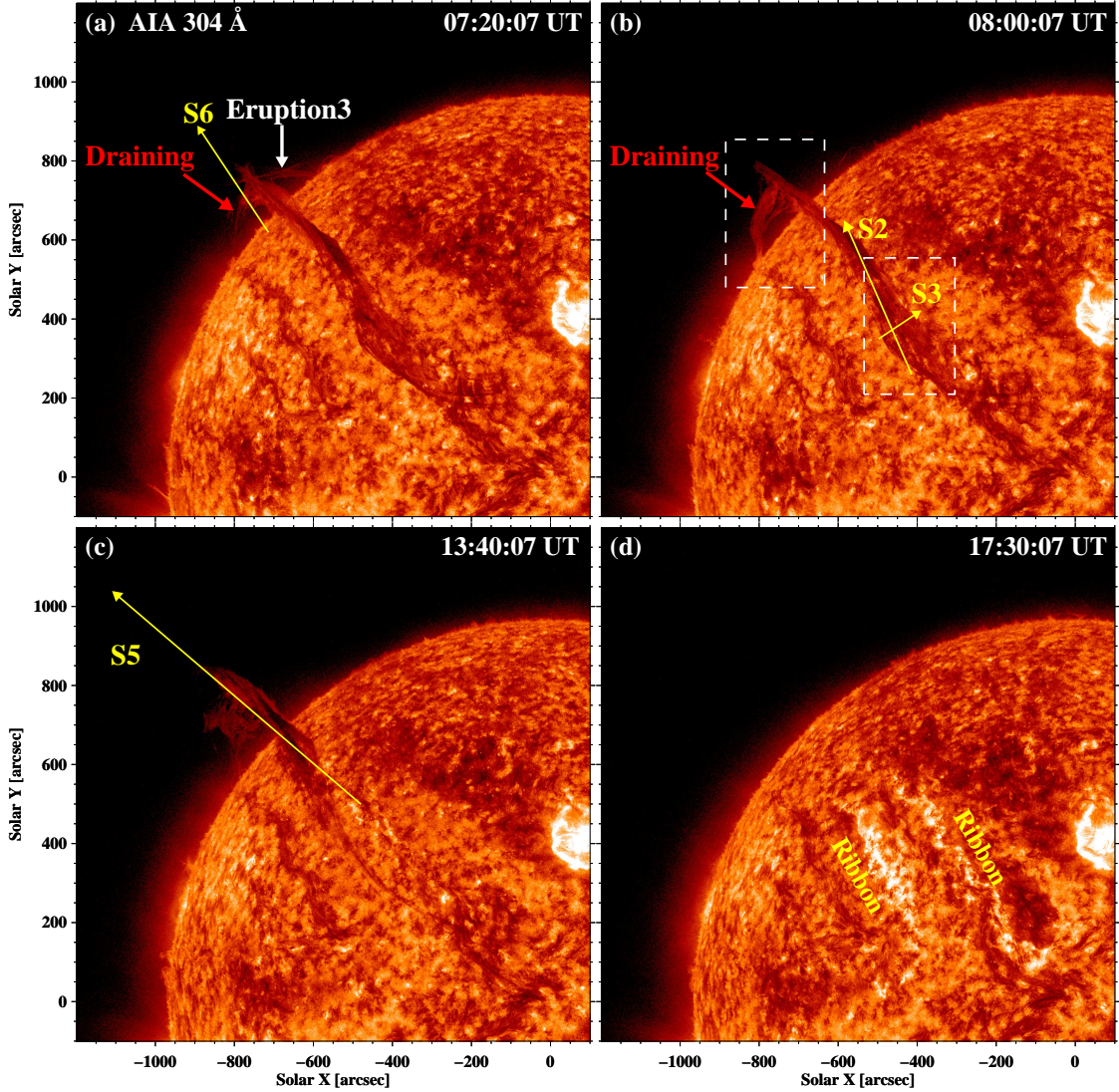


**Figure 4.** Four snapshots of AIA 304 Å images showing the mass-draining and eruption of the larger filament. The red arrows point to the mass-draining along the barb. The white arrow points to another eruption (Eruption3) near the barb, which is traced by the yellow slice S6. In panel (b), the dashed boxes denote the FOV of Figure 3(a1-a3) and Figure 3(b1-b6), respectively. The yellow slice S2 and S3 are used to investigate the longitudinal and transverse oscillations in F1. The yellow slice S5 in panel (c) is used to investigate the slow rise and fast rise of F1. An animation (*F1eruption.mp4*) of the unannotated SDO observations is available. *F1eruption.mp4* covers  $\sim 16.7$  hr starting at 00:00:07 UT and ending the same day at 16:40:31 UT, with time cadence of 1 minute.) (An animation of this figure is available.)

OS2 by  $\sim 75$  minutes and last for  $\sim 1.5$  cycles. To investigate the initiation of Eruption3, we select a straight slice (S6) with a length of  $324''$  and the time-space diagram in 304 Å is plotted in Figure 5(f). In Figure 5(b-f), the white dashed line denotes the start time of OS2 and OS4 (06:05 UT) as well as Eruption3. Therefore, OS1 started after F2 eruption while the simultaneous oscillations OS2 and OS4 started after the onset of Eruption3.

To precisely determine the parameters of oscillations in F1, we fit the curves in Figure 5(b-c) using `mpfit.pro`

and the following function:

$$A(t) = A_0 \sin\left(\frac{2\pi t}{P} + \psi\right) e^{-\frac{t}{\tau}} + A_1 t + A_2, \quad (3)$$

where  $A_0$  is the initial amplitude,  $P$  is the period,  $\tau$  is the damping time,  $\psi$  is the initial phase, and  $A_1 t + A_2$  represents a linear term of the equilibrium position of the filament threads.

In Figure 6, the four groups of crosses represent the extracted positions of the oscillating filament threads along S2 and S3 in 211 Å. The results of curve fitting using Equation 3 are overlaid with black solid lines. It



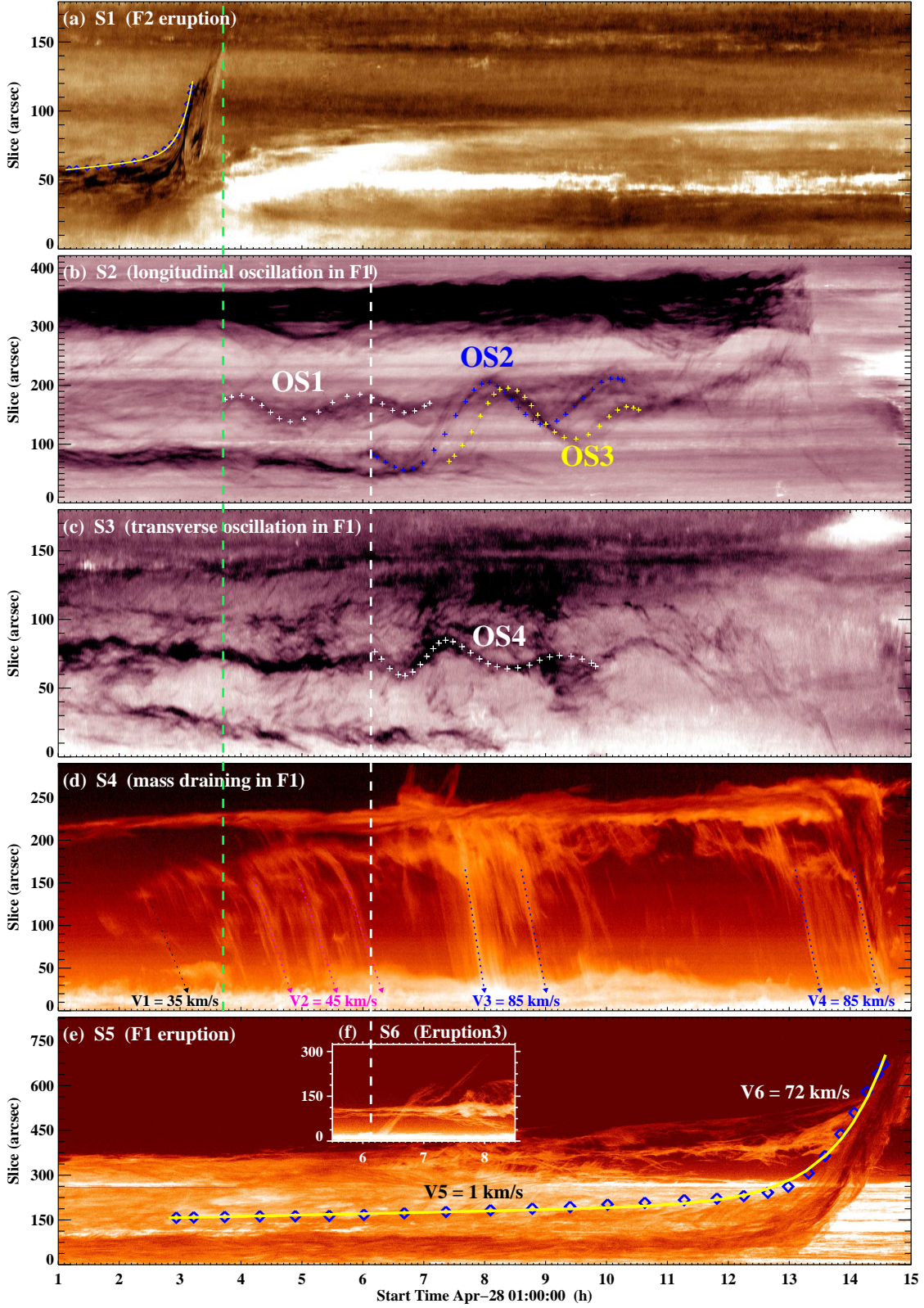


**Figure 5.** Time-space diagrams for slice S1-S6 as given in previous figures. The white, blue, and yellow dashed lines in panel (b) outline the longitudinal oscillations. The white dashed line in panel (c) outlines the transverse oscillation. The black, magenta, and blue dotted lines in panel (d) are used to calculate the apparent velocities of mass-draining at different phases. The green dashed line in panels (a-d) marks the end time of F2 eruption. The white dashed line in panels (b-f) marks the start time of the simultaneous oscillations (OS2, OS4) and Eruption3. The blue diamonds in panel (a) and (e) outline the heights of F2 and F1, and the white and yellow solid line represents the fitted curve using Equation 1. The apparent velocities during the slow rise and fast rise are labeled.

is evident that the curve fitting is satisfactory, and the fitted parameters are listed in Figure 6 and Table 1. For the longitudinal oscillations, OS1 has an amplitude of  $\sim 25.1$  Mm and a period of  $\sim 114$  min. OS2 and OS3 have displacement amplitudes of  $57 \pm 0.5$  Mm, which is  $\sim 2.3$  times larger than that of OS1. The velocity amplitudes ( $41\text{--}46$  km s $^{-1}$ ) are  $\sim 2$  times larger than that of OS1 as well. The periods (126–142 min) are roughly equal to that of OS1, implying that the curvature radius of the magnetic dips supporting the threads is similar. The damping times are between 170 min and 230 min, and the corresponding quality factor ( $\tau/P$ ) lies in the range of 1.3–1.6. The parameters for OS3 are close to those of longitudinal filament oscillation on 2015 June 29 (Zhang et al. 2017a). Different from the longitudinal oscillations (OS2, OS3), the amplitude and the velocity amplitude of the transverse oscillation OS4 are significantly smaller ( $\sim 14.7$  Mm and  $14$  km s $^{-1}$ ). OS4 has a period of  $\sim 105$  min and a damping time of  $\sim 142$  min, and the corresponding quality factor ( $\tau/P$ ) is  $\sim 1.4$ . Generally, the damping times of LATOs are in range of 25–180 minutes (tables in Tripathi et al. 2009; Shen et al. 2014a), while those of LALOs are in range of 115–600 minutes (e.g., Jing et al. 2003; Vršnak et al. 2007). Such distinction should be associated with the different damping mechanisms. The damping of LATOs may be attributed to emission of waves or various dissipative processes (Kleczeck & Kuperus 1969; Tripathi et al. 2009). The damping of LALOs are usually caused by the radiation or heat conduction, mass accretion, and wave leakage (Zhang et al. 2012, 2013; Luna & Karpen 2012; Luna et al. 2012, 2014).

### 3.3. Persistent mass-draining in F1

Figure 3(b1–b6) shows six snapshots of the EUV 304 Å images during 02:30–13:30 UT (see also online movie *OSandDR.mp4*). The feature traced by the curved line S4 in Figure 3(b3) indicates that the mass-draining along the barb of F1 toward the chromosphere took place intermittently and lasted for  $\sim 14$  hr. In order to investigate the mass-draining, we used the curved slice S4 (with a length of  $280''$ ) to construct the time-space diagram of Figure 5(d). The evolution of mass-draining is roughly divided into four phases. Before OS1, that is, from  $\sim 01:00$  UT to  $\sim 03:30$  UT, the mass-draining is discontinuous with an average velocity of  $\sim 35$  km s $^{-1}$  (black dotted line). After the onset of non-damping oscillation OS1 at  $\sim 03:35$  UT, the mass-draining becomes continuous with a slight increase in velocity (up to  $\sim 45$  km s $^{-1}$ , magenta dotted lines). It is interesting to note that the amplitude of OS2 and OS4 are larger than the preceding OS1, at which time the apparent ve-

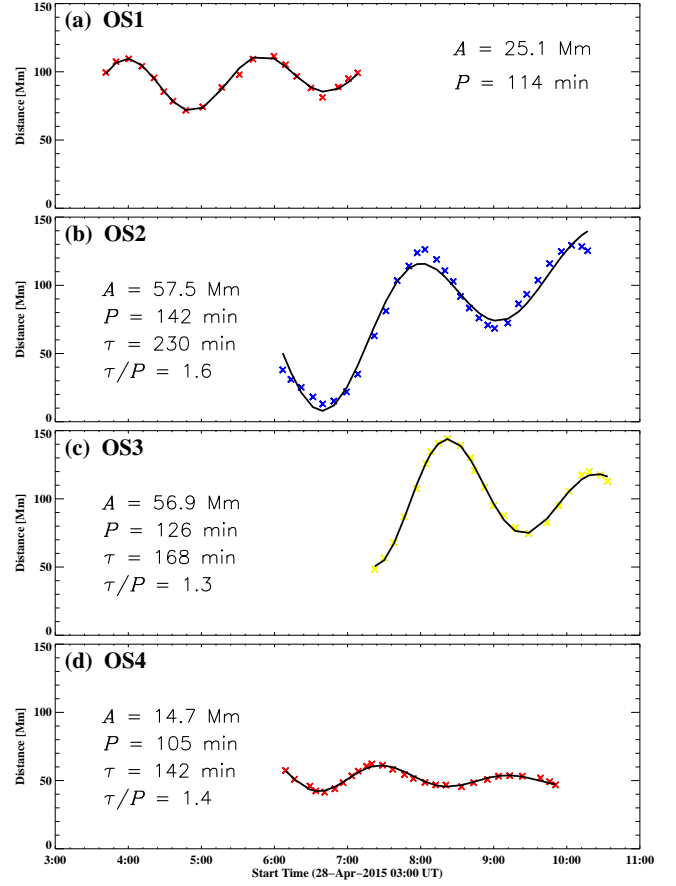


**Figure 6.** Extracted positions of the oscillating threads during OS1–OS4. The fitted curves are overlaid with black solid lines. Corresponding parameters are labeled in each panel.

locity of mass-draining enhances to  $\sim 85$  km s $^{-1}$  (blue dotted lines) during Eruption3, which is indicative of filament destabilization. During 10:00–13:00 UT, the mass-draining looks sporadic, which is due to the fact that the curved slice (S4) does not fully cover the threads guiding the mass-draining in the filament barb. Finally, the mass-draining reappear with an average velocity of  $\sim 85$  km s $^{-1}$  (blue dotted lines) during the fast rise and eruption phase of F1.

### 3.4. Eruption of F1

Finally, the longer filament F1 erupted successfully in the northeast direction (see Figure 4 and the online movie *F1eruption.mp4*). The eruption resulted in two flare ribbons as indicated in Figure 4(d), leading to a wide CME with a linear speed of  $\geq 500$  km s $^{-1}$  as observed by LASCO, in addition to significant coronal dimmings (Lřrinćk et al. 2021). In Figure 7(b1–b3), the CME associated with F1 appeared initially at  $\sim 14:29$  UT in the FOV of LASCO/C2 and expanded quickly, showing a typical three-part structure (Illing & Hund-



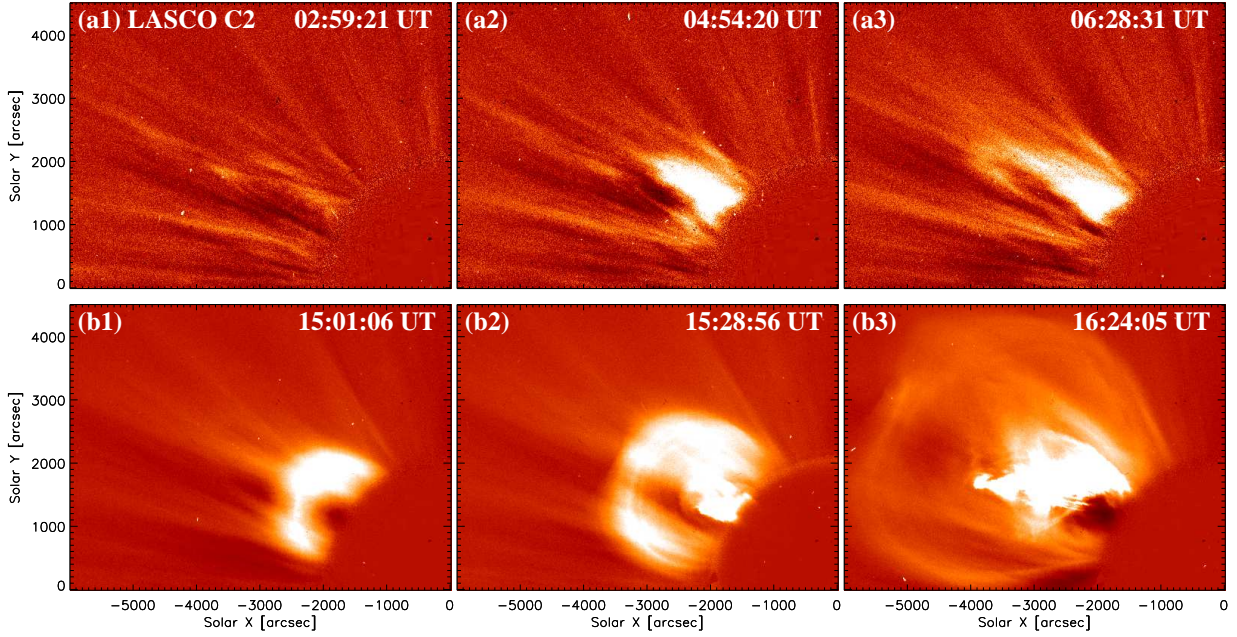


**Figure 7.** Six snapshots of the white-light CME observed by LASCO/C2. Top panels show the CME associated with F2 eruption, and bottom panels show the CME associated with F1 eruption.

hausen 1986). To investigate the early-phase kinematics of F1, we select a long straight slice (S5) with a length of  $830''$  in Figure 4(c), and its corresponding time-space diagram is shown in Figure 5(e). Likewise, the height of F1 along S5 is outlined with blue diamonds and fitted with Equation 1. The fitted curve is overlaid with the yellow solid line in Figure 5(e). It is seen that F1 started rising slowly from  $\sim 02:50$  UT with an initial speed of  $\sim 1 \text{ km s}^{-1}$ , and the slow rise lasted for  $\sim 500$  min. The onset of the fast rise occurred at  $\sim 11:10$  UT, and the average speed of fast rise is  $\sim 72 \text{ km s}^{-1}$ . In Figure 2(b) of Lörinčík et al. (2021), the labeled  $126 \text{ km s}^{-1}$  represents the final propagation speed of F1 in the FOV of AIA, which is definitely larger than the average speed, since the acceleration phase is included in our calculation.

#### 4. DISCUSSION AND CONCLUSION

##### 4.1. Sympathetic eruptions and triggering mechanism of oscillations

In this paper, we report on a sympathetic filament eruption induced by a series of nearby filament eruptions. The time interval between the first and last eruption is about 8 hours, longer than those previously reported (Shen et al. 2012; Song et al. 2020; Hou et al. 2020).

Generally, the main triggering mechanism of LALOs is sub-flares and micro-flares near the footpoints of filaments (Jing et al. 2003, 2006; Vrřnak et al. 2007; Luna & Karpen 2012; Zhang et al. 2013), although sometimes nearby filament eruption may excite LALOs (Mazumder

et al. 2020). The green dashed line in Figure 5(a-c) denotes the end of the F2 eruption (when it left the FOV at  $\sim 03:30$  UT) and the start of OS1. It is seen that the onset of OS1 in F1 is cotemporal with the end time of F2 eruption, suggesting a connection between OS1 in F1 and F2 eruption. Furthermore, the 3D magnetic field lines obtained by the PFSS modeling in Figure 8 show that the two filaments are almost under the same set of overlying magnetic field lines (marked by the yellow arrow in Figure 8), indicating the two filament are closely associated by sharing common overlying magnetic field (Cheng et al. 2005; Török et al. 2011). Therefore, the disturbance caused by the F2 eruption would propagate along the magnetic field to F1 (Jiang et al. 2008), causing the apparently non-damping LALOs in addition to the slight increase in the mass-draining rate. Noticeably, F2 eruption caused only longitudinal oscillations but no transverse oscillations, which may be due to the F2 eruption not producing shock waves (Shen et al. 2014a,b).

Generally speaking, LATOs could be triggered by the slow-rise or pre-eruption of nearby erupting filaments. (Isobe & Tripathi 2006; Isobe et al. 2007; Pintér et al. 2008; Chen et al. 2008). The white dashed line in Figure 5(b-d) denotes the initiation of Eruption3 and the simultaneous oscillations. It is obvious that Eruption3 started after the first, slightly enhanced draining, and Eruption3 is followed closely by both the simultaneous oscillations (OS2 and OS4) and another round of enhanced draining (V3) in F1. As Eruption3 was projected close to a barb of F1, the temporal coincidence

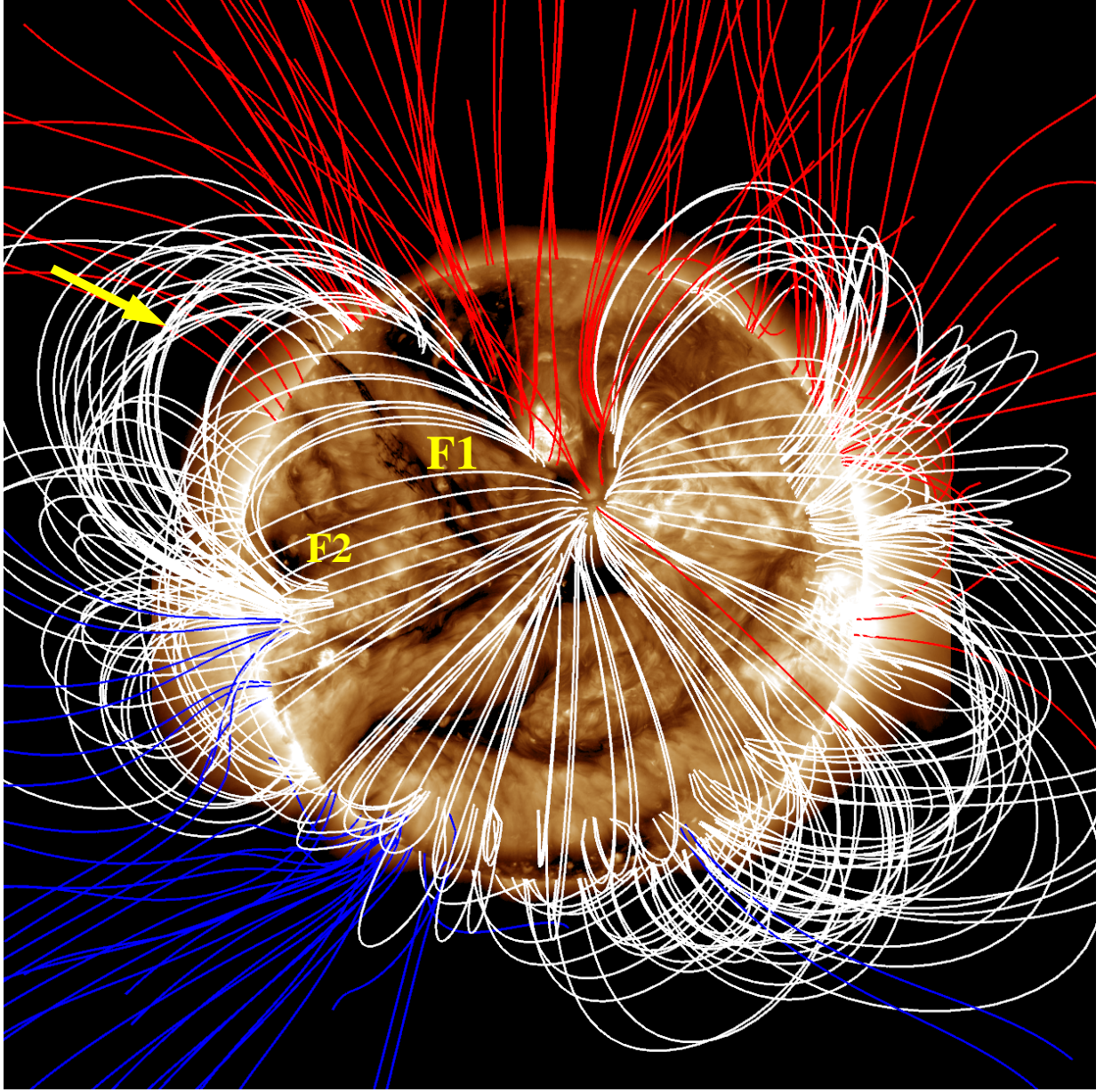


**Figure 8.** The Magnetic field lines obtained by PFSS modeling. Open and closed field lines are coded with blue/red and white lines, respectively. The image in AIA 193 Å shows F1 and F2 at 02:00:06 UT.

of the outlined series of events tentatively suggest that Eruption3 may have been involved within the global interplay and occurred in response to the (V2) draining, before contributing to the triggering of the subsequent (OS2 and OS4) oscillations and additional (V3) draining. However, without another vantage point from e.g., STEREO (Kaiser et al. 2008), we are unable to elaborate on, or even confirm, this speculative series of events. Nevertheless, in Figure 9 we draw a time line of the events, showing clearly the sequence of events potentially associated with the eruption of F1:

1. The eruption of F2 is cotemporal with the generation of LALOs and a slight increase of pre-existing mass-draining in F1. At the same time, F1 started to rise slowly.
2. The slight increase of the mass-draining precedes the Eruption3 near the barb of F1.
3. Eruption3 is followed by a significant enhancement of the mass-draining and the simultaneous oscillations in F1.
4. The persistent draining and oscillations continue up to the successful eruption of the filament F1.



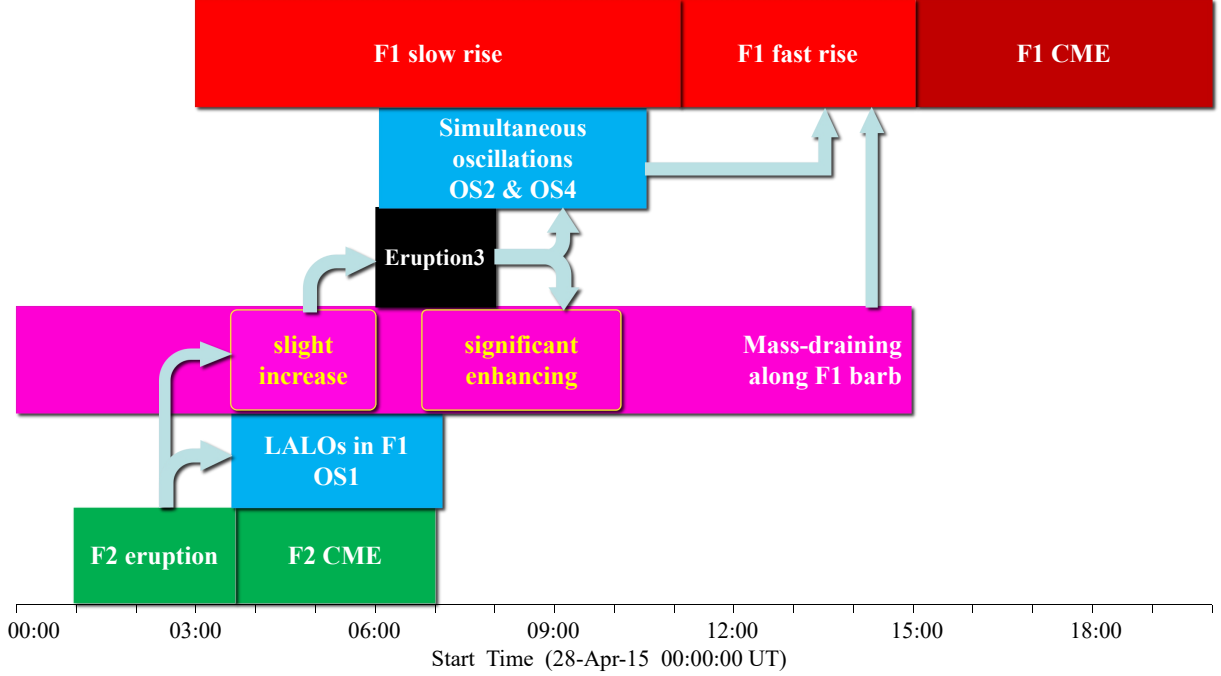


**Figure 9.** Time line of the events on 2015 April 28, including F2 eruption and the associated CME (green box), oscillations (blue boxes) and mass-draining (magenta boxes) in F1, Eruption3 (black boxes), slow rise and fast rise of F1 (red boxes), and CME related to F1 eruption (dark red boxes). The grey arrows represent cause and effect.

The complex combination of the aforementioned dynamics may be considered as the collection of processes responsible for bringing the magnetic field of the filament to a point of global instability. The trigger mechanism of F2 can not be obtained in this study due to insufficient information.

#### 4.2. Prominence seismology

Since the first report of LALOs (Jing et al. 2003), the restoring forces of LALOs have been explored extensively. Several candidates are proposed, including the magnetic pressure gradient along the filament axis (Vršnak et al. 2007; Shen et al. 2014b), magnetic tension force (Li & Zhang 2012), gas pressure gradient force (Jing et al. 2003), and projected gravity along the dip (Zhang et al. 2012). Numerical simulations have demonstrated that gravity is the dominant restoring force and the longitudinal oscillation can be well explained using a pendulum model (Luna & Karpen 2012; Luna et al. 2012; Zhang et al. 2013; Fan 2020). For the general pendulum model, the period of oscillation can be expressed as:

$$P = 2\pi\sqrt{\frac{R}{g_{\odot}}}, \quad (4)$$

where  $R$  is the curvature radius of the dip and  $g_{\odot} = 0.274 \text{ km s}^{-2}$  is the gravitational acceleration at photospheric heights. Using the observed periods of LALOs in

Table 1, the curvature radius of magnetic dip supporting F1 is estimated to be  $\sim 355 \text{ Mm}$ , which is about three times the values established in previous works (Luna et al. 2017; Zhang et al. 2017b). Besides, the transverse magnetic field strength of the dipoles can be expressed as (Luna et al. 2014):

$$B_{tr}[\text{G}] \geq 17P[\text{hr}]. \quad (5)$$

Using the observed value of  $P \approx 2 \text{ hr}$ , the magnetic field strength at the dipoles is estimated to be  $\geq 34 \text{ G}$ , which is consistent with the value for quiescent prominence derived from the flux rope insertion method (e.g. Su & van Ballegooijen 2012; Guo et al. 2021).

#### 4.3. Relationship between the longitudinal oscillations, mass-draining, and eruption

The interplay between mass drainage and longitudinal oscillation in filaments has received relatively little attention. Bi et al. (2014) reported on a filament eruption that occurred on 2012 February 23. Before the eruption, the filament underwent longitudinal oscillations with velocity amplitudes of  $54 \pm 3 \text{ km s}^{-1}$  and mass drainage toward the solar surface at a speed of  $\sim 62 \text{ km s}^{-1}$ . The displacement amplitudes of oscillations did not change, but the periods increased by 20%–30%, implying that the dipoles supporting the filament material became shallower during the oscillations as the result of continuous mass drainage.

In the current study, as indicated in Figure 5, the mass drainage along the barb started at  $\sim 01:00$  UT and lasted for  $\sim 14$  hr, which is much longer than the durations in the events reported by Bi et al. (2014) and Zhang et al. (2017b). The apparent velocity of mass unloading increased from  $\geq 35$  km s $^{-1}$  to  $\sim 45$  km s $^{-1}$ , and later enhanced to  $\sim 85$  km s $^{-1}$ . The longitudinal oscillations OS1 commenced at  $\sim 03:35$  UT, and the simultaneous oscillations (OS2, OS4) started at  $\sim 06:05$  UT, with a larger amplitude ( $\sim 57$  Mm) than OS1. It suggests there exists a relationship between the sudden and larger-amplitude oscillations and the simultaneous, increased mass-draining, but we can not ascertain whether the two accelerate each other. Simultaneous enhancements in mass drainage and oscillations may be manifestations of a gradual destabilization of F1 before its eruption.

Mass-unloading before filament eruption has been noticed in stereoscopic observations (Seaton et al. 2011). Jenkins et al. (2018) concluded that the depletion of mass from a filament leads to a lighter structure that can then rise to a height that renders the host magnetic field as torus unstable. The mass depletion reduces the total gravity of the filament and accordingly increases the upward net force that facilitates the final eruption. In this way, a positive feedback is formed. In the current study, the density of the filament was  $\sim 3.2 \times 10^{-14}$  g cm $^{-3}$  using the spectroscopic observation (Xue et al. 2021), the plane-of-sky velocity of the draining mass was between 35 to 85 km s $^{-1}$ , and the cross section of the flux tube in the barb was  $\sim 1.65 \times 10^{18}$  cm $^2$ . Assuming a filling factor of  $\sim 0.1$  for the filament material along the barb, the total mass loss during the persistent mass-draining is estimated to have been  $(1.0\text{--}2.2) \times 10^{15}$  g, which, depending on the magnitude of the photospheric field beneath the filament, may have played an essential role in triggering the eruption (Jenkins et al. 2018, 2019).

Using the spectroscopic observation of LATOs within a prominence, Chen et al. (2008) proposed that LATOs serves as a precursor of solar eruptions. Zhang et al. (2012) proposed that LATOs may also serve as a precursor, considering that the oscillation may disrupt the equilibrium by changing the plasma distribution. In current case, both mass-unloading and oscillations are observed before filament eruption. However, we can not

tell which plays a dominant role in triggering the final eruption. MHD numerical simulations are especially required to distinguish the roles (Fan 2020).

Due to the lack of stereoscopic observations of the Eruption3, we are not sure whether the slight increase of the mass-draining caused Eruption3 and whether Eruption3 fed back to enhanced the mass-draining. We only speculate on the possible close connection between them by the simultaneity of these events. Hence we hope that similar events can be observed from multiple perspectives in the future.

#### 4.4. Conclusion

In this paper, we report a sympathetic successful filament eruption induced by two nearby eruptions on 2015 April 28. We give an analysis to the multi-wavelength observations of the oscillations and mass-draining within the filament prior to its successful eruption. Non-damping longitudinal oscillation and subsequent simultaneous damping oscillations in the larger filament were cotemporal with the two eruptions, respectively. The two eruptions are also cotemporal with the enhanced transition of the pre-existing mass-draining along the barb of the filament. Such cotemporal dynamical relationship is consistent with the triggering process of the oscillations and enhanced mass-draining in previous studies. The events reported here reinforce the theory that a connection exists between the nearby eruptions and the oscillations as well as the mass-draining dynamics. In light of the contemporaneous nature of the dynamics studied here, we conclude that their interplay was ultimately responsible for the eruption of filament F1.

SDO is a mission of NASA's Living With a Star Program. AIA and HMI data are courtesy of the NASA/SDO science teams. This work is funded by NSFC grants (No. 11790302, 11790300, 11773079, 41761134088, 11473071) and the Strategic Priority Research Program on Space Science, CAS (XDA15052200, XDA15320301). Q.M.Z. is also supported by the CAS Key Laboratory of Solar Activity, National Astronomical Observatories (KLSA202006), and the International Cooperation and Interchange Program (11961131002).

#### REFERENCES

- Adrover-González, A. & Terradas, J. 2020, A&A, 633, A113. doi:10.1051/0004-6361/201936841
- Arregui, I., Oliver, R., & Ballester, J. L. 2018, Living Reviews in Solar Physics, 15, 3. doi:10.1007/s41116-018-0012-6



- Awasthi, A. K., Liu, R., & Wang, Y. 2019, *ApJ*, 872, 109.  
doi:10.3847/1538-4357/aafdad
- Ballester, J. L. 2006, *Philosophical Transactions of the Royal Society of London Series A*, 364, 405.  
doi:10.1098/rsta.2005.1706
- Bi, Y., Jiang, Y., Yang, J., et al. 2014, *ApJ*, 790, 100.  
doi:10.1088/0004-637X/790/2/100
- Bocchialini, K., Baudin, F., Koutchmy, S., et al. 2011, *A&A*, 533, A96. doi:10.1051/0004-6361/201016342
- Brueckner, G. E., Howard, R. A., Koomen, M. J., et al. 1995, *SoPh*, 162, 357. doi:10.1007/BF00733434
- Chen, P. F., Innes, D. E., & Solanki, S. K. 2008, *A&A*, 484, 487. doi:10.1051/0004-6361:200809544
- Chen, P. F. 2011, *Living Reviews in Solar Physics*, 8, 1.  
doi:10.12942/lrsp-2011-1
- Cheng, J.-X., Fang, C., Chen, P.-F., et al. 2005, *ChJA&A*, 5, 265. doi:10.1088/1009-9271/5/3/006
- Cheng, X., Zhang, J., Ding, M. D., et al. 2013, *ApJL*, 769, L25. doi:10.1088/2041-8205/769/2/L25
- Dai, J., Ji, H., Li, L., et al. 2021, *ApJ*, 906, 66.  
doi:10.3847/1538-4357/abcaf4
- Ding, J. Y., Hu, Y. Q., & Wang, J. X. 2006, *SoPh*, 235, 223. doi:10.1007/s11207-006-0092-7
- Fan, Y. 2020, *ApJ*, 898, 34. doi:10.3847/1538-4357/ab9d7f
- Forbes, T. G., Linker, J. A., Chen, J., et al. 2006, *SSRv*, 123, 251. doi:10.1007/s11214-006-9019-8
- Gibson, S. E. 2018, *Living Reviews in Solar Physics*, 15, 7.  
doi:10.1007/s41116-018-0016-2
- Gilbert, H. R., Holzer, T. E., & Burkepile, J. T. 2001, *ApJ*, 549, 1221. doi:10.1086/319444
- Guo, J., Zhou, Y., Guo, Y., et al. 2021, *arXiv:2107.12181*
- Hou, Y. J., Li, T., Song, Z. P., et al. 2020, *A&A*, 640, A101.  
doi:10.1051/0004-6361/202038348
- Huang, C. J., Guo, J. H., Ni, Y. W., et al. 2021, *arXiv:2104.13546*
- Hyder, C. L. 1966, *ZA*, 63, 78
- Illing, R. M. E. & Hundhausen, A. J. 1986, *J. Geophys. Res.*, 91, 10951.  
doi:10.1029/JA091iA10p10951
- Isobe, H. & Tripathi, D. 2006, *A&A*, 449, L17.  
doi:10.1051/0004-6361:20064942
- Isobe, H., Tripathi, D., Asai, A., et al. 2007, *SoPh*, 246, 89.  
doi:10.1007/s11207-007-9091-6
- Janvier, M., Aulanier, G., & Démoulin, P. 2015, *SoPh*, 290, 3425. doi:10.1007/s11207-015-0710-3
- Jenkins, J. M., Long, D. M., van Driel-Gesztelyi, L., et al. 2018, *SoPh*, 293, 7. doi:10.1007/s11207-017-1224-y
- Jenkins, J. M., Hopwood, M., Démoulin, P., et al. 2019, *ApJ*, 873, 49. doi:10.3847/1538-4357/ab037a
- Ji, H., Wang, H., Schmahl, E. J., et al. 2003, *ApJL*, 595, L135. doi:10.1086/378178
- Jiang, Y., Shen, Y., Yi, B., et al. 2008, *ApJ*, 677, 699.  
doi:10.1086/529417
- Jin, M., Schrijver, C. J., Cheung, M. C. M., et al. 2016, *ApJ*, 820, 16. doi:10.3847/0004-637X/820/1/16
- Jing, J., Lee, J., Spirock, T. J., et al. 2003, *ApJL*, 584, L103. doi:10.1086/373886
- Jing, J., Lee, J., Spirock, T. J., et al. 2006, *SoPh*, 236, 97.  
doi:10.1007/s11207-006-0126-1
- Joshi, N. C., Schmieder, B., Magara, T., et al. 2016, *ApJ*, 820, 126. doi:10.3847/0004-637X/820/2/126
- Kaiser, M. L., Kucera, T. A., Davila, J. M., et al. 2008, *SSRv*, 136, 5. doi:10.1007/s11214-007-9277-0
- Kleczeck, J. & Kuperus, M. 1969, *SoPh*, 6, 72.  
doi:10.1007/BF00146797
- Labrosse, N., Heinzel, P., Vial, J.-C., et al. 2010, *SSRv*, 151, 243. doi:10.1007/s11214-010-9630-6
- Lemen, J., Title, A., Akin, D., et al. 2012, *SoPh*, 275, 17.  
doi:10.1007/s11207-011-9776-8
- Li, T. & Zhang, J. 2012, *ApJL*, 760, L10.  
doi:10.1088/2041-8205/760/1/L10
- Liakh, V., Luna, M., & Khomenko, E. 2020, *A&A*, 637, A75. doi:10.1051/0004-6361/201937083
- Liakh, V., Luna, M., & Khomenko, E. 2021, *arXiv:2108.01143*
- Liu, C., Lee, J., Karlický, M., et al. 2009, *ApJ*, 703, 757.  
doi:10.1088/0004-637X/703/1/757
- Liu, R., Liu, C., Xu, Y., et al. 2013, *ApJ*, 773, 166.  
doi:10.1088/0004-637X/773/2/166
- Low, B. C. 1996, *SoPh*, 167, 217. doi:10.1007/BF00146338
- Lörincik, J., Dudík, J., Aulanier, G., et al. 2021, *ApJ*, 906, 62. doi:10.3847/1538-4357/abc8f6
- Luna, M. & Karpen, J. 2012, *ApJL*, 750, L1.  
doi:10.1088/2041-8205/750/1/L1
- Luna, M., Díaz, A. J., & Karpen, J. 2012, *ApJ*, 757, 98.  
doi:10.1088/0004-637X/757/1/98
- Luna, M., Knizhnik, K., Muglach, K., et al. 2014, *ApJ*, 785, 79. doi:10.1088/0004-637X/785/1/79
- Luna, M., Su, Y., Schmieder, B., et al. 2017, *ApJ*, 850, 143.  
doi:10.3847/1538-4357/aa9713
- Luna, M., Karpen, J., Ballester, J. L., et al. 2018, *ApJS*, 236, 35. doi:10.3847/1538-4365/aabde7
- Luna, M. & Moreno-Insertis, F. 2021, *ApJ*, 912, 75.  
doi:10.3847/1538-4357/abec46
- Lynch, B. J. & Edmondson, J. K. 2013, *AGU Fall Meeting Abstracts*
- Mackay, D. H., Karpen, J. T., Ballester, J. L., et al. 2010, *SSRv*, 151, 333. doi:10.1007/s11214-010-9628-0

- Martin, S. F. 1998, *SoPh*, 182, 107.  
doi:10.1023/A:1005026814076
- Mazumder, R., Pant, V., Luna, M., et al. 2020, *A&A*, 633, A12. doi:10.1051/0004-6361/201936453
- Moon, Y.-J., Choe, G. S., Park, Y. D., et al. 2002, *ApJ*, 574, 434. doi:10.1086/340945
- Moore, R. L., Sterling, A. C., Hudson, H. S., et al. 2001, *ApJ*, 552, 833. doi:10.1086/320559
- Moreton, G. E. & Ramsey, H. E. 1960, *PASP*, 72, 357.  
doi:10.1086/127549
- Okamoto, T. J., Nakai, H., Keiyama, A., et al. 2004, *ApJ*, 608, 1124. doi:10.1086/420838
- Oliver, R. & Ballester, J. L. 2002, *SoPh*, 206, 45.  
doi:10.1023/A:1014915428440
- Oliver, R. 2009, *SSRv*, 149, 175.  
doi:10.1007/s11214-009-9527-4
- Pant, V., Srivastava, A. K., Banerjee, D., et al. 2015, *Research in Astronomy and Astrophysics*, 15, 1713.  
doi:10.1088/1674-4527/15/10/008
- Parenti, S. 2014, *Living Reviews in Solar Physics*, 11, 1.  
doi:10.12942/lrsp-2014-1
- Pintér, B., Jain, R., Tripathi, D., et al. 2008, *ApJ*, 680, 1560. doi:10.1086/588273
- Pesnell, W., Thompson, B., & Chamberlin, P. 2012, *SoPh*, 275, 3
- Régnier, S., Walsh, R. W., & Alexander, C. E. 2011, *A&A*, 533, L1. doi:10.1051/0004-6361/201117381
- Ramsey, H. E. & Smith, S. F. 1966, *AJ*, 71, 197.  
doi:10.1086/109903
- Ruderman, M. S. & Luna, M. 2016, *A&A*, 591, A131.  
doi:10.1051/0004-6361/201628713
- Schou, J., Scherrer, P., Bush, R., et al. 2012, *SoPh*, 275, 229. doi:10.1007/s11207-011-9842-2
- Schrijver, C. J. & Title, A. M. 2011, *Journal of Geophysical Research (Space Physics)*, 116, A04108.  
doi:10.1029/2010JA016224
- Schrijver, C. J., Title, A. M., Yeates, A. R., et al. 2013, *ApJ*, 773, 93. doi:10.1088/0004-637X/773/2/93
- Schrijver, C. J. & De Rosa, M. L. 2003, *SoPh*, 212, 165.  
doi:10.1023/A:1022908504100
- Seaton, D. B., Mierla, M., Berghmans, D., et al. 2011, *ApJL*, 727, L10. doi:10.1088/2041-8205/727/1/L10
- Shen, Y., Liu, Y., & Su, J. 2012, *ApJ*, 750, 12.  
doi:10.1088/0004-637X/750/1/12
- Shen, Y., Ichimoto, K., Ishii, T. T., et al. 2014, *ApJ*, 786, 151. doi:10.1088/0004-637X/786/2/151
- Shen, Y., Liu, Y. D., Chen, P. F., et al. 2014, *ApJ*, 795, 130. doi:10.1088/0004-637X/795/2/130
- Shen, Y., Liu, Y., Tian, Z., et al. 2017, *ApJ*, 851, 101.  
doi:10.3847/1538-4357/aa9af0
- Song, Z., Hou, Y., Zhang, J., et al. 2020, *ApJ*, 892, 79.  
doi:10.3847/1538-4357/ab77b3
- Su, Y. & van Ballegooijen, A. 2012, *ApJ*, 757, 168.  
doi:10.1088/0004-637X/757/2/168
- Terradas, J., Soler, R., Luna, M., et al. 2015, *ApJ*, 799, 94.  
doi:10.1088/0004-637X/799/1/94
- Titov, V. S., Mikic, Z., Török, T., et al. 2012, *ApJ*, 759, 70.  
doi:10.1088/0004-637X/759/1/70
- Török, T. & Kliem, B. 2005, *ApJL*, 630, L97.  
doi:10.1086/462412
- Török, T., Panasenco, O., Titov, V. S., et al. 2011, *ApJL*, 739, L63. doi:10.1088/2041-8205/739/2/L63
- Tripathi, D., Isobe, H., & Jain, R. 2009, *SSRv*, 149, 283.  
doi:10.1007/s11214-009-9583-9
- van Ballegooijen, A. A. & Martens, P. C. H. 1989, *ApJ*, 343, 971. doi:10.1086/167766
- Vršnak, B., Veronig, A. M., Thalmann, J. K., et al. 2007, *A&A*, 471, 295. doi:10.1051/0004-6361:20077668
- Wang, H., Chae, J., Yurchyshyn, V., et al. 2001, *AGU Spring Meeting Abstracts*
- Wang, R., Liu, Y. D., Hu, H., et al. 2016, *AGU Fall Meeting Abstracts*
- Wang, D., Liu, R., Wang, Y., et al. 2018, *ApJ*, 869, 177.  
doi:10.3847/1538-4357/aaef35
- Wheatland, M. S. & Craig, I. J. D. 2006, *SoPh*, 238, 73.  
doi:10.1007/s11207-006-0206-2
- Xue, J., Li, H., & Su, Y. 2021, *arXiv:2109.02908*
- Zhang, Q. M., Chen, P. F., Xia, C., et al. 2012, *A&A*, 542, A52. doi:10.1051/0004-6361/201218786
- Zhang, Q. M., Chen, P. F., Xia, C., et al. 2013, *A&A*, 554, A124. doi:10.1051/0004-6361/201220705
- Zhang, Q. M., Li, D., & Ning, Z. J. 2017a, *ApJ*, 851, 47.  
doi:10.3847/1538-4357/aa9898
- Zhang, Q. M., Li, T., Zheng, R. S., et al. 2017b, *ApJ*, 842, 27. doi:10.3847/1538-4357/aa73d2
- Zhang, Q. M. & Ji, H. S. 2018, *ApJ*, 860, 113.  
doi:10.3847/1538-4357/aac37e
- Zhang, L. Y., Fang, C., & Chen, P. F. 2019, *ApJ*, 884, 74.  
doi:10.3847/1538-4357/ab3d3a
- Zhang, Q. M., Guo, J. H., Tam, K. V., et al. 2020, *A&A*, 635, A132. doi:10.1051/0004-6361/201937291
- Zhang, Q., Liu, R., Wang, Y., et al. 2021, *arXiv:2108.09401*
- Zhou, Y.-H., Zhang, L.-Y., Ouyang, Y., et al. 2017, *ApJ*, 839, 9. doi:10.3847/1538-4357/aa67de
- Zhou, Y.-H., Xia, C., Keppens, R., et al. 2018, *ApJ*, 856, 179. doi:10.3847/1538-4357/aab614
- Zhukov, A. N. & Veselovsky, I. S. 2007, *ApJL*, 664, L131.  
doi:10.1086/520928